



Roughness, inertia, and diffusion effects on anomalous transport in rough channel flows

Seonkyoo Yoon ¹ and Peter K. Kang ^{1,2,*}¹*Department of Earth and Environmental Sciences, University of Minnesota, Minneapolis, Minnesota 55455, USA*²*Saint Anthony Falls Laboratory, University of Minnesota, Minneapolis, Minnesota 55455, USA*

(Received 21 May 2019; accepted 6 January 2021; published 29 January 2021)

We study how the complex interplay between channel roughness, inertia, and diffusion controls tracer transport in rough channel flows. We first simulate flow and tracer transport over wide ranges of channel roughness, Reynolds number (Re), and Péclet number (Pe) observable in nature. Pe exerts a first-order control on first-passage time distributions, and the effect of roughness on the tracer transport becomes evident as Re increases. The interplay between the roughness and Re causes recirculating flows, which intensify or suppress anomalous transport depending on Pe . At infinite Pe , the late-time scaling follows a universal power-law scaling, which is explained by conducting a scaling analysis. With extensive numerical simulations and stochastic modeling, we show that the roughness, inertia, and diffusion effects are encoded in Lagrangian velocity statistics represented by velocity distribution and velocity correlation. We successfully reproduce anomalous transport using an upscaled stochastic model that honors the key Lagrangian velocity statistics.

DOI: [10.1103/PhysRevFluids.6.014502](https://doi.org/10.1103/PhysRevFluids.6.014502)

I. INTRODUCTION

Fluid flow and mass transport in rough-walled channels are ubiquitous phenomena occurring in numerous engineering applications and natural processes, including microfluidics, biomedical devices, heat exchangers, and fractured geological media [1–7]. Quantifying and predicting solute transport in channel flows are essential for the effective design and optimization of these various applications. For example, contaminant transport in fractured geological media is fundamentally governed by flow and solute transport in rough channels (fractures), and quantifying solute spreading in fractured media is essential for the risk assessment of contaminated fractured aquifers and the design of underground nuclear waste repositories. Since Taylor's seminal work on solute dispersion in shear flows [8], many studies have proposed various methods to quantify the effective dispersion in more complex flow fields [9–21]. Although these effective dispersion approaches are useful in capturing solute transport in many applications, the Fickian regime is often not reached and anomalous transport, often manifested by the power-law tailing of tracer breakthrough curves and the nonlinear scaling of second spatial moments, that cannot be captured by Taylor dispersion are widely observed [22–31]. The solute transport in rough channel flows is a representative example of such preasymptotic systems [17,32–34].

Recent studies highlighted the importance of inertia effects (Re) and medium heterogeneity on initiating nonlinear flows and anomalous transport in porous and fractured media [27,35–37]. For example, the critical Re that initiates vortical flows is shown to vary more than three orders

*Corresponding author: pkkang@umn.edu

of magnitude depending on the pore-scale heterogeneity [36], and flow and transport behavior at channel intersections are proven to be sensitive to Re and the roughness of channel walls [38]. Also, the interplay between inertia effects (Re) and the medium heterogeneity is shown to fundamentally change both flow and transport processes [27,37]. A key manifestation of inertia effects in channel flows is the emergence of recirculation zones, and recent studies on tracer transport through rough channel flows revealed the importance of recirculation zones on solute transport: recirculation zones are shown to trap solute particles and cause heavy tailing of tracer breakthrough curves [35,39–41]. However, the effects of recirculating flows were investigated for specific channel geometries and over relatively narrow ranges of Reynolds number (Re) and Péclet number (Pe). In practice, the roughness, inertia, and diffusion effects can vary over wide ranges, potentially leading to complex transport behaviors [27,38,42,43]. For example, the trapping mechanism induced by the diffusion of solute particles into recirculation zones should strongly depend on Pe, and the occurrence of recirculation zones are governed by both channel geometries and Re. However, we currently lack a systematic study that comprehensively investigates the combined effects of channel roughness, Re, and Pe on flow and transport in rough channel flows. This limits our ability to predict and control transport processes in channel flow systems.

In this study, we elucidate how the complex interplay between channel roughness, inertia, and diffusion effects governs the tracer transport in rough channel flows by combining high-performance numerical simulations, stochastic modeling, and scaling analysis. We first independently vary channel roughness, Re, and Pe over wide ranges and conduct high-performance numerical simulations to generate comprehensive data set on fluid flow and tracer transport. We systematically analyze the obtained tracer breakthrough curves and quantify the effects of recirculation zones on anomalous transport. We then elucidate channel roughness, inertia, and diffusion effects on Lagrangian velocity statistics and parametrize an upscaled transport model with key Lagrangian velocity statistics.

II. FLUID FLOW AND SOLUTE TRANSPORT IN ROUGH CHANNELS

Rough surfaces are ubiquitous in nature, and there are various measures that quantify the surface roughness [44,45]. We consider self-affine rough walls, as rough surfaces in nature are often found to be statistically self-affine [46–49]. Self-affine surfaces are scale-invariant in that the standard deviation of the height difference Δz between two points separated by lateral distance Δx can be expressed as $\sigma_{\Delta z}(\Delta x) = \lambda^{-H} \sigma_{\Delta z}(\lambda \Delta x)$, and H is the Hurst exponent that characterizes the surface roughness [32,50]. We investigate the roughness effects on flow and transport by varying the Hurst exponent (H) in the range of 0.7–0.9, which is consistent with that observed in nature [7,32,51]. We use the successive random addition algorithm [50,52] to generate rough surfaces of length $L = 10$ cm. The generated rough surfaces are duplicated and detached to have a constant aperture of 1 mm, which is comparable to the roughness amplitude. Figure 1(a) shows examples of generated rough channels. By varying H , we can systematically vary the ratio between the roughness length scale and the aperture, which is a key factor that determines the roughness effects on flow and transport [32,53]. We also confirmed that the root mean square of the surface height values increases as H decreases. Note that natural fractures often show a significant aperture variability [54]. Although we do not explicitly consider the aperture variability, the surface roughness introduces the variability in effective hydraulic aperture [55,56].

We investigate the inertia effects on tracer transport by varying the Reynolds number defined as $\text{Re} = \frac{ub}{\nu}$, and investigate the diffusion effects on tracer transport by varying the Péclet number defined as $\text{Pe} = \frac{ub}{2D}$. u is the average fluid velocity, b is the aperture, ν is the kinematic viscosity of the fluid, and D is the molecular diffusivity. We consider seven different inertia regimes: $\text{Re} = [1, 10, 20, 40, 60, 80, 100]$, and five different Pe regimes: $\text{Pe} = [10^2, 10^3, 10^4, 10^5, \infty]$. $\text{Pe} = \infty$ implies that the tracer transport is purely advective with zero diffusion coefficient, $D = 0$. We fix u and vary Pe by varying D and vary Re by varying ν . We choose Pe and Re ranges such that they cover the observable Schmidt number, $\text{Sc} = \frac{\text{Pe}}{\text{Re}}$, in nature [1,57]. Therefore, this study is not limited

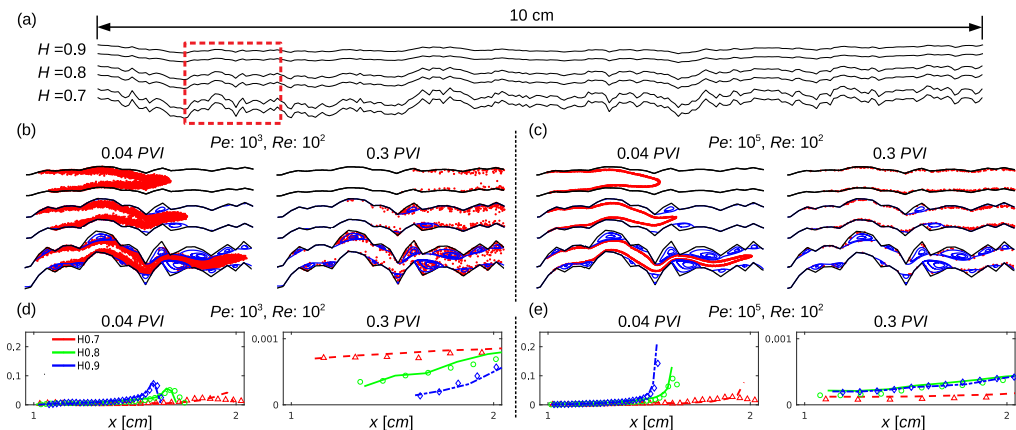


FIG. 1. (a) Rough channels with three different Hurst exponents (H). The channel roughness increases as H decreases. (b), (c) Tracer locations between $x = 1$ cm and $x = 2$ cm at pore volume injections (PVI) of 0.04 and 0.3 are indicated using red circles for $Pe = [10^3, 10^5]$ at $Re = 100$, and recirculation zones and streamlines inside them are indicated with blue lines. (d), (e) Projected tracer concentration profiles at 0.04 and 0.3 PVI for $Pe = [10^3, 10^5]$ at $Re = 100$. The symbols indicate the CTRW predictions for $H = 0.7$ (triangles), $H = 0.8$ (circles), and $H = 0.9$ (diamonds).

to a specific solute or solvent, and considers various solute-solvent combinations under various thermal conditions.

We simulate a Newtonian fluid flow by solving steady-state incompressible Navier–Stokes equations for rough channels using the finite volume method [58]. A constant flux boundary condition is imposed on the left boundary of the channel, and a zero-pressure gradient boundary condition is imposed on the right boundary. We discretize the channel with a resolution of 0.002 mm, yielding $50,000 \times 500$ grid cells within the channel domain.

We simulate passive solute transport using a particle tracking method [59]. The advective transport is simulated using a streamline-based particle tracking algorithm that considers no-slip boundary conditions at solid–fluid interfaces [60]. The diffusive displacement is modeled using a random walk method: a particle jumps $\sqrt{4D\Delta t}$ in a random direction over time-step Δt [61]. The Lagrangian method is free of numerical dispersion and can accurately simulate particle transport at high Pe regimes. We inject 10^4 particles in each realization with a flux-weighted line injection. To avoid undesired inlet and outlet boundary effects, we inject tracers 1 cm away from the inlet boundary and measure the arrival times of tracers 1 cm from the outlet boundary. Thus, the total longitudinal (x -directional) travel distance is 8 cm.

In summary, to establish the comprehensive understanding of tracer transport in rough channels, we simulate the flow and solute transport by varying H , Re , and Pe independently over wide ranges: $H = [0.7, 0.8, 0.9]$, $Re = [1, 10, 20, 40, 60, 80, 100]$, and $Pe = [10^2, 10^3, 10^4, 10^5, \infty]$. The independent variation of H , Re , and Pe helps discern the role of each factor. To avoid being case-specific, we simulate an ensemble of 10 realizations for each combination of H , Re , and Pe . Therefore, the total number of flow and transport simulations is $10 \times \#(H) \times \#(Re) \times \#(Pe) = 10 \times 3 \times 7 \times 5 = 1050$. We made use of the cutting-edge high-performance computing resources at the Minnesota Supercomputing Institute to meet the considerable computational cost requirements for this purpose.

III. SIMULATION RESULTS AND SCALING ANALYSIS

To highlight the complex interplay, we first present the effects of H and Pe on tracer transport at $Re = 100$. As shown in Figs. 1(b) and 1(c), an increase in the roughness increases the size and frequency of the recirculation zones. The role of recirculation zones on tracer transport is sensitive

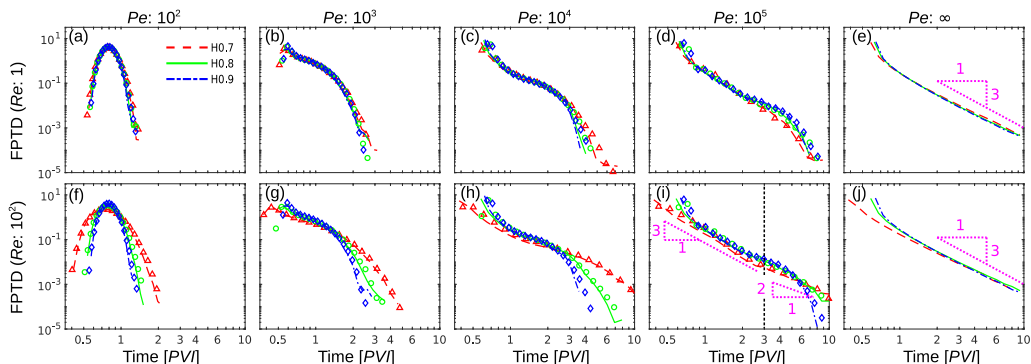


FIG. 2. First-passage time distributions (FPTDs) at $x = 9$ cm. The presented FPTDs are ensemble averages over 10 realizations. The lines indicate the FPTDs from direct simulations, and the symbols indicate the CTRW predictions for $H = 0.7$ (triangles), $H = 0.8$ (circles), and $H = 0.9$ (diamonds). At $Pe = \infty$, the FPTDs show a universal scaling of -3 .

to Pe . At $Pe = 10^3$, tracers readily diffuse into recirculation zones, and the recirculation zones trap these tracers. Interestingly, the recirculation zones play the opposite role at $Pe = 10^5$. At $Pe = 10^5$, the tracers can no longer easily enter the recirculation zones, and the recirculation zones rather facilitate tracer transport near the channel walls. See Supplemental Material for videos showing tracer transport simulations at $Pe = 10^3$ and 10^5 [62]. This is because the dividing streamlines that separate the recirculation zones and the main flow channel effectively act as slip boundaries at high Pe . This effect is clearly manifested in the projected concentration profiles at pore volume injection (PVI) of 0.3, as shown in Figs. 1(d) and 1(e), where one PVI is the time duration required to inject fluid as much as one pore volume of a channel. The tailing in the projected concentration profile becomes stronger with the increase in the roughness at $Pe = 10^3$; however, the trend is opposite at $Pe = 10^5$. The tailing decreases as the roughness increases at $Pe = 10^5$.

The normalized breakthrough curves or first-passage time distributions (FPTDs) for the various combinations of H , Re , and Pe are shown in Fig. 2. First, note that Pe is the most significant factor in determining the overall shapes of the FPTDs. The effects of roughness on FPTDs are minimal at low Re (the first row of Fig. 2) and only become evident at higher Re (the second row of Fig. 2). The overall shapes of FPTDs are most sensitive to Pe . We focus on two key characteristics of the anomalous transport: early arrival and late-time tailing in the FPTDs. We observe an enhanced early arrival as both the roughness and Re increase. A high roughness coupled with significant inertial effects (high Re) causes recirculation zones to enlarge. We delineate recirculation zones based on the mass balance principle [63], and calculate the ratio between the total area of recirculation zones and the channel domain area for all H - Re combinations as shown in Fig. 3(a). While the ratio is zero (i.e., no recirculating flows) regardless of Re in smooth channels ($H = 0.9$), the ratio increases as Re increases for rough channels ($H = 0.7, 0.8$). As shown in Fig. 1, the enlarged recirculating flows narrow the mobile zone (the main flow channel), and the decreased cross-sectional area of the main flow channel leads to an overall increase in the velocity along the main flow channel [63]. This explains the enhanced early arrival of the tracers at high roughness and high Re , as shown in Fig. 2.

The late-time behavior of the FPTDs is determined by the particles traveling through low-velocity regions. No-slip boundary conditions and recirculation zones create low-velocity regions near the channel walls. To quantify the trapping effects of recirculating flows on FPTD, we subtract particle residence times spent in recirculation zones from first passage times. From the delineation of recirculation zones and the Lagrangian particle trajectories obtained from the particle tracking method, we can calculate the total time spent in recirculation zones for each particle trajectory. This allows us to directly quantify the contribution of recirculation zones on the total residence

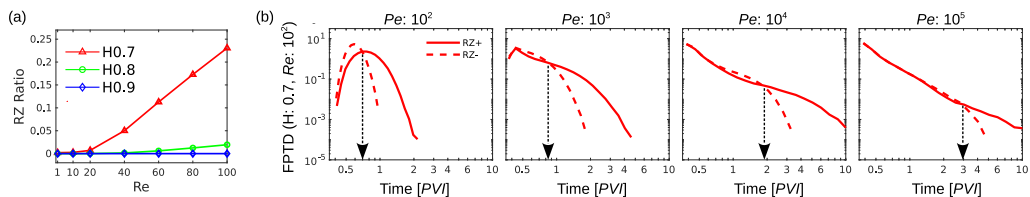


FIG. 3. (a) The area ratio between the recirculation zones (RZ) and the channel domain. Recirculation zones enlarge as the channel roughness and Re increases. (b) Comparison between the FPTD at $H = 0.7$ (RZ +) and the residence time of the tracers only in the main channels (RZ -) where RZ stands for recirculation zones. The residence times of particles in the main channels are calculated by subtracting the particle residence times in recirculation zones from the first-passage times.

times of solutes. The red dashed lines in Fig. 3(b) show the distributions of subtracted first passage times (first passage times subtracted by total residence times in recirculation zones) at $H = 0.7$ and $Re = 100$ and clearly demonstrate trapping effects. As Pe increases, the trapping effects are observed much later (see black dashed arrows). This indicates that the contribution of recirculating flows to late-time tailing emerges at later times as Pe increases.

In Fig. 2, for $Pe = 10^5$, we can observe that the FPTD of $H = 0.7$ case decays faster than $H = [0.8, 0.9]$ upto $t \sim 3$ PVI as shown in Fig. 2(i). More than 99% solute particles breakthrough before 3 PVI. This implies that, the larger recirculation zones for $H = 0.7$ case aid the transit of most particles at high Pe regimes. This is because the particles cannot easily enter the recirculation zones due to the limited diffusion, and the recirculating zones do not delay but rather aid the transit of the particles by acting as slip boundaries and by reducing effective flow area. Consequently, the FPTDs in the smoother cases (e.g., $H = [0.8, 0.9]$) show stronger tailing than that in the $H = 0.7$ case up to $t \sim 3$ PVI [Fig. 2(i)]. This observation is consistent with the projected tracer concentration profiles [Figs. 1(d) and (e)]. Although fewer particles are captured at high Pe regimes, once captured, the trapped particles stay longer inside the recirculation zones compared with that observed at lower Pe regimes. This explains the change in scaling at PVI ~ 3 in Fig. 2(i) and the rightmost column of Fig. 3(b).

At $Pe = \infty$, the late-time scaling of the FPTDs shows a universal power-law scaling of t^{-3} for all combinations of Pe, Re, and H [Figs. 2(e) and 2(j)]. We perform a scaling analysis to explain the observed universal power-law scaling. The low-velocity regions should determine the late-time scaling, and the tracers at $Pe = \infty$ cannot enter the recirculation zones. Thus, we hypothesize that the late-time scaling at $Pe = \infty$ is determined by the no-slip boundary conditions. For a Poiseuille flow with an aperture b , the velocity profile across the channel follows the parabolic equation $u(y) = 6qb^{-3}[(b/2)^2 - y^2]$, where q is the constant influx into the channel. The Eulerian velocity probability density function (PDF) corresponding to the parabolic profile is given as follows [64]:

$$f_e(u) = -\frac{2}{b} \frac{dy}{du} = \frac{1}{6q\sqrt{\frac{1}{4b^2} - \frac{u}{6qb}}}. \quad (1)$$

The PDF of the Lagrangian velocities is related to the Eulerian velocity PDF through flux weighting as $f_{\mathcal{L}}(u) = \frac{uf_e(u)}{\int du uf_e(u)}$ [65]. The late-time scaling of the FPTD, $f_t(t)$, should be determined by the distribution of the low velocities in $f_{\mathcal{L}}(u)$. Since t is a random variable proportional to the reciprocal of the random variable u , the late-time scaling of $f_t(t)$ follows that of the inverse distribution of u as [66]

$$f_t(t) \propto \frac{1}{t^2} f_{\mathcal{L}}\left(\frac{1}{t}\right) \propto \frac{1}{t^3} \cdot \frac{1}{\sqrt{c_1 - c_2/t}}, \quad (2)$$

where $c_1 = (4b^2)^{-1}$ and $c_2 = (6qb)^{-1}$. For large t , we obtain $f_t(t) \propto t^{-3}$. This confirms that the no-slip boundary condition indeed governs the late-time scaling at infinite Pe regardless of the roughness and Re.

IV. LAGRANGIAN VELOCITY STATISTICS

Recent studies reported that pore structures govern underlying velocity distributions and pore-scale velocities are strongly correlated [24,37,59,64,67–69]. Also, the effective transport in porous media has been successfully characterized by considering the interplay between the velocity distribution and the velocity correlation [26,40,65,70–72]. For channel flows, the roughness of the wall can lead to a significant difference in velocity between the main channel flow and the near-wall low-velocity zones, causing a broad velocity distribution [43,73,74]. Moreover, the Lagrangian velocities sampled along a particle trajectory in the channel flows should retain the memory of the prior velocities because of the mass conservation constraint. A natural conjecture is that Lagrangian velocity statistics will capture the compound effects of H , Re, and Pe on anomalous transport.

We characterize the Lagrangian velocity statistics using the Lagrangian velocity PDF (velocity distribution) and velocity correlation. We first quantify the motion of the solute particles in equidistance, Δx , in the mean flow direction. The velocity distribution is characterized using the PDF of the transition time $\tau = \frac{\Delta x}{v}$, where v is the average Lagrangian velocity over Δx which incorporates both the advective and diffusive motions of particles. The transition times are sampled at every $\Delta x = 1$ mm from all the particle trajectories. Herein, we refer to the PDF of the transition times as the Transition Time Distribution (TTD). We characterize the Lagrangian velocity correlation by quantifying the velocity correlation lengths conditional to initial velocity values. At preasymptotic regimes, velocity correlation can strongly depend on the initial velocity values [75,76]. We classify the initial Lagrangian velocities into 10 classes, wherein each class is equidistantly spaced in a log-scale. Based on the initial log-velocity values, the particles are assigned into one of the 10 classes, $i = [1, \dots, 10]$, where $i = 10$ is the class with the highest velocities. We estimate the characteristic correlation length for each class i as $\ell_i = \int_0^L C(x|i)/C(0|i)dx$, where $C(x|i) = \int_{-\infty}^{\infty} |P(\log v|i, x) - P(\log v, L)|d \log v$ [75]. Here, $P(\log v|i, x)$ is the conditional log-velocity distribution for particles belonging to class i , and $P(\log v, L)$ is the marginal log-velocity distribution at the outlet.

The underlying mechanisms of the early arrival and late-time tailing are effectively captured in the TTDs (Fig. 4) and velocity correlation (Fig. 5). We first discuss the early arrival behavior. The probability of having short transition times (high-velocity) increases with the increase in the roughness and Re (Fig. 4). This implies that the flow channeling effect is encoded in the TTDs. The channeling effect is also encoded in the correlation length (Fig. 5). The correlation length of the velocity class $i = 10$ controls the early arrival of the tracers, and we observe that, for $i = 10$, the correlation length in the $H = 0.7$ case is larger than those in the smoother cases as Re increases [Fig. 5(c)]. Recirculation zones, which enlarge with the increase in Re [Fig. 3(a)], reduce the cross-sectional flow area and cause a strong preferential path (Fig. 1). The strong preferential flow reduces the velocity fluctuation and thereby increases the velocity correlation. The higher probability of having higher velocities combined with a strong velocity correlation explains the early arrival behavior at $H = 0.7$, Re = 100.

Similar to the early arrival behavior, the late-time behavior is also encoded in the TTDs and velocity correlation. To quantify the tail of the TTDs, we fit the tail to a generalized Pareto distribution $G_{\xi, \sigma, \theta}(\tau) = \frac{1}{\sigma} (1 + \frac{\xi(\tau - \theta)}{\sigma})^{-1 - \frac{1}{\xi}}$, of which the support is $\tau > \theta$ when $\xi > 0$ or for $\theta < \tau < \theta - \sigma/\xi$ when $\xi < 0$. The rationale for the use of the generalized Pareto distribution is based on the Pickands–Balkema–de Haan theorem [77,78], which states that for a large class of distributions, the conditional distribution of values exceeding a certain high threshold converges to a generalized Pareto distribution [79]. We use the generalized Pareto distribution as a way to quantify late-time tailing. The three parameters θ , σ , and ξ are the location, scale, and shape parameters, respectively, and estimated using the maximum likelihood method. The threshold θ is set as the 0.9

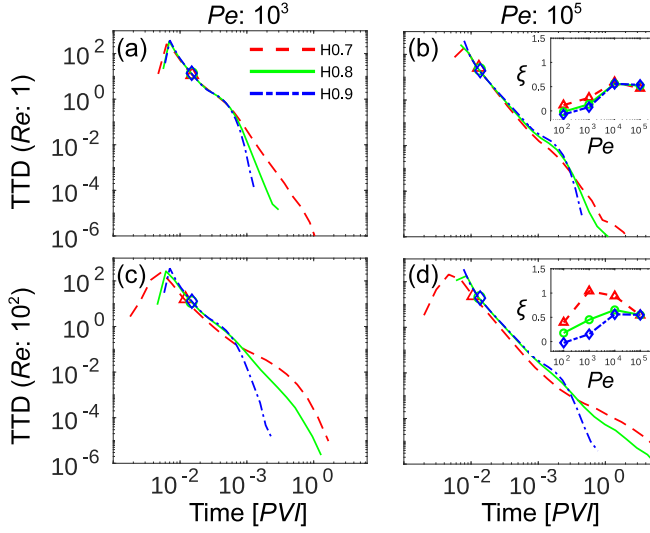


FIG. 4. Transition time distributions (TTDs) for different Pe and Re combinations. The 0.9 quantiles are indicated using triangles for $H = 0.7$, circles for $H = 0.8$, and diamonds for $H = 0.9$. Insets: tail index ξ as a function of Pe and H at (b) $Re = 1$ and (d) $Re = 100$. ξ quantifies the heavy-tailedness.

quantile, i.e., $\tau_{0.9}$, of the cumulative distribution of the transition times. The scale parameter σ can be related to the smallest and the largest transition times. The shape parameter ξ , often called the tail index, quantifies the heaviness of a tail (the greater the value of ξ , the heavier the tail) [80]. Note that the method of maximum likelihood finds the parameter values that maximizes the likelihood function $\mathcal{L}(\xi, \sigma, \theta | \mathbf{t})$ where $\mathbf{t} = \{\tau | \tau \geq \tau_{0.9}\}$.

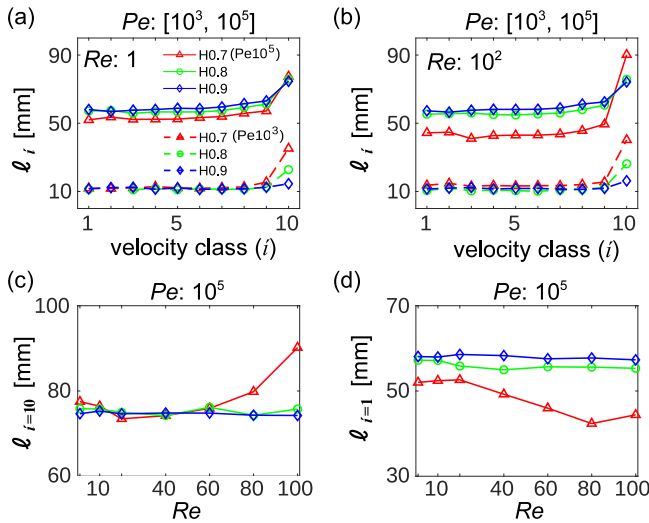


FIG. 5. Conditional velocity correlation lengths for $Pe = [10^3, 10^5]$ at (a) $Re = 1$ and (b) $Re = 100$. Correlation length increases with the increase in Pe and velocity class. (c) Evolution of ℓ_i as a function of Re at $Pe = 10^5$ for the velocity class $i = 10$ and (d) $i = 1$. For $H = 0.7$, $\ell_{i=10}$ increases as Re increases, and $\ell_{i=1}$ decreases as Re increases. This behavior is well correlated with the increase in the relative area of the recirculation zones [Fig. 3(a)].

The insets in Fig. 4 show the estimates of the tail index. When recirculating flows are strong ($H = 0.7$, $\text{Re} = 100$), the tail index significantly increases with the increase in Pe from 100 to 10^3 [inset of Fig. 4(d)]. This is due to the stronger trapping effect at $\text{Pe} = 10^3$. At $\text{Pe} = 100$, the particles easily enter the recirculation zones but also easily exit. When Pe increases beyond 10^3 , the tail index decreases significantly at $H = 0.7$, confirming that the particles cannot efficiently sample velocities in the recirculation zones.

Not only the transition times but also the velocity correlation determines the late-time behavior. The role of velocity correlation on the late-time behavior can be highlighted from the trend of $\ell_{i=1}$ as a function of Re at $H = 0.7$. At high Pe regimes, the particles traveling near the walls will alternate between low (no-slip wall) and relatively high (recirculation zone interface) velocities, thus decreasing the velocity correlation. For the low velocity class $i = 1$, the correlation length indeed decreases with the increase in Re at $\text{Pe} = 10^5$ and $H = 0.7$ [Fig. 5(d)], confirming the effect of recirculation zones acting as slip boundary conditions. This trend is also well correlated with the increase in the relative area of recirculation zones as a function of Re [Fig. 3(a)].

The decreased tailing in the TTDs (due to less trapping effects) and the loss of velocity correlation (induced by the slip boundaries) explain how recirculation zones suppress the anomalous transport at high Pe . Finally, the role of Pe in determining the overall shape of the FPTD is also evident from the TTDs and velocity correlation. Pe has a strong effect on both TTD and velocity correlation, whereas the roughness at $\text{Re} = 1$ has little effect on both the TTD [inset of Fig. 4(b)] and velocity correlation [Fig. 5(a)]. In summary, the effects of roughness, inertia, and diffusion on effective transport are evident in Lagrangian velocity distribution and velocity correlation.

V. UPSCALED STOCHASTIC TRANSPORT MODEL

We hypothesize that the complex H - Re - Pe interplay in rough channels is effectively encoded in velocity distribution and velocity correlation, which in turn determine the effective transport. To test our hypothesis, we quantify the effective tracer transport using an upscaled model that only takes the velocity distribution and correlation as input parameters. The continuous time random walk model with one-step velocity correlation, often referred to as the spatial Markov model (SMM), has been successfully applied to predict anomalous transport across spatial scales including pore scales [24,68], network scales [26,81], and Darcy scales [70].

We test the hypothesis by running the spatial Markov model as an effective transport model. The effective particle transport can be characterized using the Langevin equations,

$$x^{(n+1)} = x^{(n)} + \Delta x, \quad t^{(n+1)} = t^{(n)} + \tau^{(n)}, \quad (3)$$

where $\{\tau^{(n)} = \frac{\Delta x}{v^{(n)}}\}_{n=0}^{L/\Delta x}$ is a series of transition times. The transition time, $\tau^{(n)}$, in Eq. (3) is modeled as a Markov chain, whose transitions can be characterized using a transition matrix. We sample the Lagrangian velocity transitions at every $\Delta x = 5$ mm, which is smaller than the estimated correlation length (Fig. 5). We classify $\{v^{(n)}\}_{n=0}^{L/\Delta x}$ into 10 classes equidistantly spaced in a log-scale, and then construct the transition matrix T_{ij} , which characterizes the transition probability from class i to class j . Although we parameterized the spatial Markov model using the pore-scale simulation results, the model could also be constructed from more practical information such as breakthrough curves [82] and geostatistical properties of media [83]. Recent studies also showed that the transition matrix could be efficiently parametrized with only one or two parameters [65,76,84]. However, the efficient parametrization of SMM is not the focus of this study. The spatial Markov model accurately predicts the projected concentrations and FPTDs for all combinations of H , Re , and Pe [Figs. 1(d), 1(e) and 2]. This confirms the hypothesis that the H - Re - Pe interplay is effectively encoded in the velocity distribution and correlation and that they are sufficient for quantifying the effective transport.

We also present model predictions that do not consider the velocity correlation between successive jumps, as shown in Fig. 6. The model accurately captures FPTDs at low Pe , but the

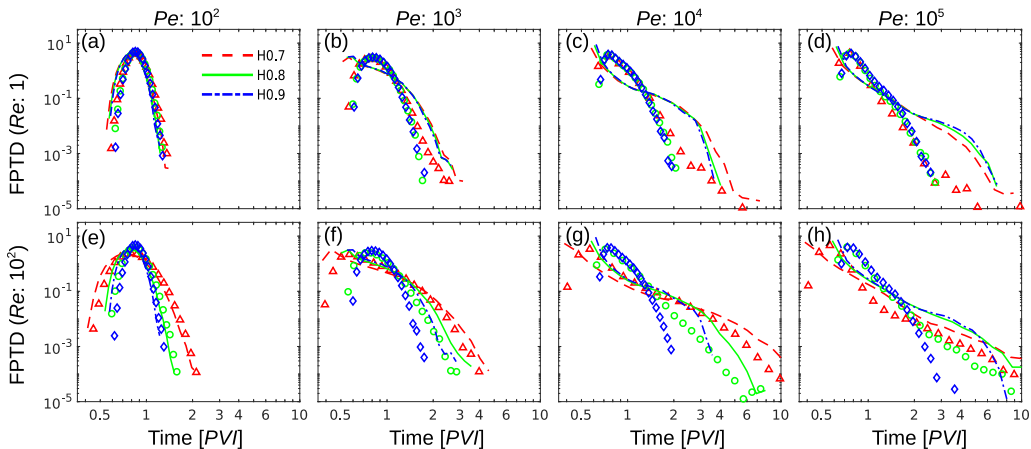


FIG. 6. FPTDs from direct numerical simulations (lines) and model predictions with no velocity correlation between successive jumps (symbols) for $H = 0.7$ (triangles), $H = 0.8$ (circles), and $H = 0.9$ (diamonds).

model fails to capture FPTDs as Pe increases. The velocity correlation increases as Pe increases, and this is why the model performance deteriorates significantly as Pe increases. Interestingly, the model without velocity correlation still well captures late-time tailing of $H = 0.7$, $Re = 100$, $Pe = 10^4$, and $Pe = 10^5$ cases [Figs. 6(g) and 6(h)]. This is because the recirculation zones at high Pe reduce low-velocity correlation by acting as slip boundary conditions, as discussed in the previous section [Fig. 5(d)]. This result highlights the importance of velocity correlation in controlling effective transport, and the model predictions are consistent with the velocity correlation structure characterized in the previous section.

VI. CONCLUSIONS AND OUTLOOK

In this study, we successfully established a mechanistic understanding of roughness (H), inertia (Re), and diffusion (Pe) effects on solute transport in rough channel flows. Wide ranges of H , Re , and Pe observable in nature were investigated, and Pe is shown to exert major control over first-passage time distributions. The effect of roughness on the tracer transport becomes evident as Re increases, and the interplay between the roughness and Re is shown to cause recirculating flows. We combined the recirculation zone delineation method with the particle tracking algorithm to quantify the effects of recirculation zones on solute transport. Through this analysis, we could quantitatively analyze and understand the role of recirculation zones on anomalous transport and found that recirculating flows can either induce or nonintuitively suppress the anomalous transport depending on the Pe value. For $Pe = \infty$ regime, we observed the universal power-law scaling, t^{-3} , in FPTDs. Using a scaling analysis, we showed that no-slip boundary conditions at channel walls determine the scaling even for high Re and rough channel cases.

Based on the improved understanding, we effectively captured anomalous transport over wide ranges of H , Re , and Pe with a stochastic model that honors the interplay between velocity distribution and correlation. A key finding of this study is that the effects of channel roughness, inertia, and diffusion are effectively encoded in Lagrangian velocity statistics, and the identified Lagrangian velocity statistics are sufficient to effectively capture solute transport in rough channel flows. This result implies that the effective transport model can potentially be directly parameterized from the information of a medium heterogeneity (e.g., channel roughness), Re , and Pe . This study should provide insights into the development of such powerful parametrization. This study investigated limited channel geometries and assumed a constant aperture, but we expect that the key findings in this study will be valid for various other geometries. For example, the aperture variability will make

the recirculation zones to more readily occur [74], and this implies that the increase in geometrical complexity will in general have similar effects as the decrease in H . A more comprehensive study on channel geometry effects on solute transport should be an important next step.

This study investigated two-dimensional (2D) systems, and 2D rough channels are relevant in many real systems when the variation of roughness in one direction is significantly larger than the other direction, such as fault surfaces with slickenlines [85], corrugated channels [6], and microfluidic devices [86]. Therefore, the results of this study are applicable to various systems. Also, we were able to comprehensively explore the compound effects of H , Re , and Pe by limiting our study to 2D. However, recent studies revealed that three-dimensional effects could exert distinctive impacts on flow and transport processes [38,43], and the extension of this study to 3D will be an important next step. Last, the excellent performance of the stochastic model shows a promise for extending the model to upscale *reactive* transport in rough channel flows [4,87].

ACKNOWLEDGMENTS

The authors gratefully acknowledge support from the Korea Environment Industry & Technology Institute (KEITI) through the Subsurface Environment Management (SEM) Project (Grant No. 2020002440002). P.K.K. also acknowledges the College of Science & Engineering at the University of Minnesota and the George and Orpha Gibson Endowment for its generous support of Hydrogeology. We thank the Minnesota Supercomputing Institute (MSI) at the University of Minnesota for computational resources and support.

-
- [1] A. D. Stroock, S. K. W. Dertinger, A. Ajdari, I. Mezić, H. A. Stone, and G. M. Whitesides, Chaotic mixer for microchannels, *Science* **295**, 647 (2002).
 - [2] T. M. Squires and S. R. Quake, Microfluidics: Fluid physics at the nanoliter scale, *Rev. Mod. Phys.* **77**, 977 (2005).
 - [3] E. K. Sackmann, A. L. Fulton, and D. J. Beebe, The present and future role of microfluidics in biomedical research, *Nature* **507**, 181 (2014).
 - [4] T. Sherman, A. Paster, G. Porta, and D. Bolster, A spatial Markov model for upscaling transport of adsorbing-desorbing solutes, *J. Contam. Hydrol.* **222**, 31 (2019).
 - [5] G. L. Morini, Single-phase convective heat transfer in microchannels: A review of experimental results, *Int. J. Therm. Sci.* **43**, 631 (2004).
 - [6] D. R. Sawyers, M. Sen, and H.-C. Chang, Heat transfer enhancement in three-dimensional corrugated channel flow, *Int. J. Heat Mass Transfer* **41**, 3559 (1998).
 - [7] B. Berkowitz, Characterizing flow and transport in fractured geological media: A review, *Adv. Water Resour.* **25**, 861 (2002).
 - [8] G. I. Taylor, Dispersion of soluble matter in solvent flowing slowly through a tube, *Proc. R. Soc. London A* **219**, 186 (1953).
 - [9] R. Aris, On the dispersion of a solute in a fluid flowing through a tube, *Proc. R. Soc. London A* **235**, 67 (1956).
 - [10] J. Koplik, J. R. Banavar, and J. F. Willemsen, Molecular Dynamics of Poiseuille Flow and Moving Contact Lines, *Phys. Rev. Lett.* **60**, 1282 (1988).
 - [11] O. Plumb and S. Whitaker, Dispersion in heterogeneous porous media: 1. Local volume averaging and large-scale averaging, *Water Resour. Res.* **24**, 913 (1988).
 - [12] I. Frankel and H. Brenner, On the foundations of generalized Taylor dispersion theory, *J. Fluid Mech.* **204**, 97 (1989).
 - [13] A. Sarracino, F. Cecconi, A. Puglisi, and A. Vulpiani, Nonlinear Response of Inertial Tracers in Steady Laminar Flows: Differential and Absolute Negative Mobility, *Phys. Rev. Lett.* **117**, 174501 (2016).

- [14] R. L. Detwiler, H. Rajaram, and R. J. Glass, Solute transport in variable-aperture fractures: An investigation of the relative importance of Taylor dispersion and macrodispersion, *Water Resour. Res.* **36**, 1611 (2000).
- [15] L. W. Gelhar and C. L. Axness, Three-dimensional stochastic analysis of macrodispersion in aquifers, *Water Resour. Res.* **19**, 161 (1983).
- [16] G. Drazer and J. Koplik, Tracer dispersion in two-dimensional rough fractures, *Phys. Rev. E* **63**, 056104 (2001).
- [17] J. Bouquain, Y. Méheust, D. Bolster, and P. Davy, The impact of inertial effects on solute dispersion in a channel with periodically varying aperture, *Phys. Fluids* **24**, 083602 (2012).
- [18] K. J. Måløy, J. Feder, F. Boger, and T. Jøssang, Fractal Structure of Hydrodynamic Dispersion in Porous Media, *Phys. Rev. Lett.* **61**, 2925 (1988).
- [19] M. S. Bello, R. Rezzonico, and P. G. Righetti, Use of Taylor-Aris dispersion for measurement of a solute diffusion coefficient in thin capillaries, *Science* **266**, 773 (1994).
- [20] E. Guyon, Y. Pomeau, J. P. Hulin, and C. Baudet, Dispersion in the presence of recirculation zones, *Nucl. Phys. B: Proc. Suppl.* **2**, 271 (1987).
- [21] J.-P. Bouchaud and A. Georges, Anomalous diffusion in disordered media: Statistical mechanisms, models and physical applications, *Phys. Rep.* **195**, 127 (1990).
- [22] B. Bijeljic and M. J. Blunt, Pore-scale modeling and continuous time random walk analysis of dispersion in porous media, *Water Resour. Res.* **42**, W01202 (2006).
- [23] S. P. Neuman and D. M. Tartakovsky, Perspective on theories of non-Fickian transport in heterogeneous media, *Adv. Water Resour.* **32**, 670 (2009).
- [24] P. de Anna, T. Le Borgne, M. Dentz, A. M. Tartakovsky, D. Bolster, and P. Davy, Flow Intermittency, Dispersion, and Correlated Continuous Time Random Walks in Porous Media, *Phys. Rev. Lett.* **110**, 184502 (2013).
- [25] T. Le Borgne, D. Bolster, M. Dentz, P. de Anna, and A. Tartakovsky, Effective pore-scale dispersion upscaling with a correlated continuous time random walk approach, *Water Resour. Res.* **47**, W12538 (2011).
- [26] P. K. Kang, T. Le Borgne, M. Dentz, O. Bour, and R. Juanes, Impact of velocity correlation and distribution on transport in fractured media: Field evidence and theoretical model, *Water Resour. Res.* **51**, 940 (2015).
- [27] A. Nissan and B. Berkowitz, Inertial Effects on Flow and Transport in Heterogeneous Porous Media, *Phys. Rev. Lett.* **120**, 054504 (2018).
- [28] J. H. Cushman and T. R. Ginn, Fractional advection-dispersion equation: A classical mass balance with convolution-Fickian flux, *Water Resour. Res.* **36**, 3763 (2000).
- [29] D. A. Benson, R. Schumer, M. M. Meerschaert, and S. W. Wheatcraft, Fractional dispersion, Lévy motion, and the MADE tracer tests, *Transp. Porous Media* **42**, 211 (2001).
- [30] K. Singha, F. D. Day-Lewis, and J. W. Lane Jr, Geoelectrical evidence of bicontinuum transport in groundwater, *Geophys. Res. Lett.* **34**, L12401 (2007).
- [31] B. Berkowitz and H. Scher, Anomalous Transport in Random Fracture Networks, *Phys. Rev. Lett.* **79**, 4038 (1997).
- [32] G. Drazer, H. Auradou, J. Koplik, and J. P. Hulin, Self-Affine Fronts in Self-Affine Fractures: Large and Small-Scale Structure, *Phys. Rev. Lett.* **92**, 014501 (2004).
- [33] G. Gioia and F. A. Bombardelli, Scaling and Similarity in Rough Channel Flows, *Phys. Rev. Lett.* **88**, 014501 (2001).
- [34] M. Giona, A. Adrover, S. Cerbelli, and F. Garofalo, Laminar dispersion at high Péclet numbers in finite-length channels: Effects of the near-wall velocity profile and connection with the generalized Leveque problem, *Phys. Fluids* **21**, 123601 (2009).
- [35] M. B. Cardenas, D. T. Slotke, R. A. Ketcham, and J. M. Sharp, Effects of inertia and directionality on flow and transport in a rough asymmetric fracture, *J. Geophys. Res.* **114**, B06204 (2009).
- [36] B. P. Muljadi, M. J. Blunt, A. Q. Raeini, and B. Bijeljic, The impact of porous media heterogeneity on non-Darcy flow behaviour from pore-scale simulation, *Adv. Water Resour.* **95**, 329 (2016).

- [37] E. Crevacore, T. Tosco, R. Sethi, G. Boccardo, and D. L. Marchisio, Recirculation zones induce non-Fickian transport in three-dimensional periodic porous media, *Phys. Rev. E* **94**, 053118 (2016).
- [38] S. H. Lee and P. K. Kang, Three-Dimensional Vortex-Induced Reaction Hot Spots at Flow Intersections, *Phys. Rev. Lett.* **124**, 144501 (2020).
- [39] D. F. Boutt, G. Grasselli, J. T. Fredrich, B. K. Cook, and J. R. Williams, Trapping zones: The effect of fracture roughness on the directional anisotropy of fluid flow and colloid transport in a single fracture, *Geophys. Res. Lett.* **33**, L21402 (2006).
- [40] D. Bolster, Y. Méheust, T. Le Borgne, J. Bouquain, and P. Davy, Modeling preasymptotic transport in flows with significant inertial and trapping effects—the importance of velocity correlations and a spatial Markov model, *Adv. Water Resour.* **70**, 89 (2014).
- [41] L. Wang and M. B. Cardenas, Non-Fickian transport through two-dimensional rough fractures: Assessment and prediction, *Water Resour. Res.* **50**, 871 (2014).
- [42] M. E. Thompson and S. R. Brown, The effect of anisotropic surface roughness on flow and transport in fractures, *J. Geophys. Res. Solid Earth* **96**, 21923 (1991).
- [43] S. H. Lee, I. W. Yeo, K.-K. Lee, and R. L. Detwiler, Tail shortening with developing eddies in a rough-walled rock fracture, *Geophys. Res. Lett.* **42**, 6340 (2015).
- [44] M. W. Smith, Roughness in the earth sciences, *Earth Sci. Rev.* **136**, 202 (2014).
- [45] M. Wang, Y.-F. Chen, G.-W. Ma, J.-Q. Zhou, and C.-B. Zhou, Influence of surface roughness on nonlinear flow behaviors in 3D self-affine rough fractures: Lattice Boltzmann simulations, *Adv. Water Resour.* **96**, 373 (2016).
- [46] B. B. Mandelbrot, *The Fractal Geometry of Nature* (Freeman, New York, 1983).
- [47] J. Kertesz, V. K. Horvath, and F. Weber, Self-affine rupture lines in paper sheets, *Fractals* **1**, 67 (1993).
- [48] L. Ponsón, D. Bonamy, and E. Bouchaud, Two-Dimensional Scaling Properties of Experimental Fracture Surfaces, *Phys. Rev. Lett.* **96**, 035506 (2006).
- [49] B. Ghanbarian, E. Perfect, and H.-H. Liu, A geometrical aperture–width relationship for rock fractures, *Fractals* **27**, 1940002 (2019).
- [50] H.-H. Liu, G. S. Bodvarsson, S. Lu, and F. J. Molz, A corrected and generalized successive random additions algorithm for simulating fractional Levy motions, *Math. Geol.* **36**, 361 (2004).
- [51] E. Bouchaud, G. Lapasset, and J. Planès, Fractal dimension of fractured surfaces: A universal value? *Europhys. Lett.* **13**, 73 (1990).
- [52] R. F. Voss, *Fractals in Nature: From Characterization to Simulation* (Springer, New York, 1988).
- [53] A. Neuville, R. Toussaint, and J. Schmittbuhl, Hydrothermal coupling in a self-affine rough fracture, *Phys. Rev. E* **82**, 036317 (2010).
- [54] N. Huang, R. Liu, Y. Jiang, B. Li, and L. Yu, Effects of fracture surface roughness and shear displacement on geometrical and hydraulic properties of three-dimensional crossed rock fracture models, *Adv. Water Resour.* **113**, 30 (2018).
- [55] S. Ge, A governing equation for fluid flow in rough fractures, *Water Resour. Res.* **33**, 53 (1997).
- [56] V. V. Mourzenko, J.-F. Thovert, and P. M. Adler, Permeability of a single fracture; validity of the Reynolds equation, *J. Phys. II France* **5**, 465 (1995).
- [57] J. Delgado, A critical review of dispersion in packed beds, *Heat Mass Transf.* **42**, 279 (2006).
- [58] OPENFOAM, The open source CFD toolbox, <http://www.openfoam.com> (2011).
- [59] B. Bijeljic, P. Mostaghimi, and M. J. Blunt, Signature of Non-Fickian Solute Transport in Complex Heterogeneous Porous Media, *Phys. Rev. Lett.* **107**, 204502 (2011).
- [60] J. P. Nunes, B. Bijeljic, and M. Blunt, Time-of-flight distributions and breakthrough curves in heterogeneous porous media using a pore-scale streamline tracing algorithm, *Transp. Porous Media* **109**, 317 (2015).
- [61] P. Mostaghimi, B. Bijeljic, and M. Blunt, Simulation of flow and dispersion on pore-space images, *SPE J.* **17**, 1 (2012).
- [62] See Supplemental Material at <http://link.aps.org/supplemental/10.1103/PhysRevFluids.6.014502> for videos showing tracer transport simulations.
- [63] J. Q. Zhou, L. Wang, Y. F. Chen, and M. B. Cardenas, Mass transfer between recirculation and main flow zones: Is physically based parameterization possible? *Water Resour. Res.* **55**, 345 (2019).

- [64] P. de Anna, B. Quaife, G. Biroso, and R. Juanes, Prediction of the low-velocity distribution from the pore structure in simple porous media, *Phys. Rev. Fluids* **2**, 124103 (2017).
- [65] M. Dentz, P. K. Kang, A. Comolli, T. Le Borgne, and D. R. Lester, Continuous time random walks for the evolution of Lagrangian velocities, *Phys. Rev. Fluids* **1**, 074004 (2016).
- [66] G. Casella and R. L. Berger, *Statistical Inference* (Duxbury, Pacific Grove, CA, 2002), Vol. 2.
- [67] S. S. Datta, H. Chiang, T. S. Ramakrishnan, and D. A. Weitz, Spatial Fluctuations of Fluid Velocities in Flow Through a Three-Dimensional Porous Medium, *Phys. Rev. Lett.* **111**, 064501 (2013).
- [68] P. K. Kang, P. de Anna, J. P. Nunes, B. Bijeljic, M. J. Blunt, and R. Juanes, Pore-scale intermittent velocity structure underpinning anomalous transport through 3-D porous media, *Geophys. Res. Lett.* **41**, 6184 (2014).
- [69] M. Carrel, V. L. Morales, M. Dentz, N. Derlon, E. Morgenroth, and M. Holzner, Pore-scale hydrodynamics in a progressively bioclogged three-dimensional porous medium: 3-D particle tracking experiments and stochastic transport modeling, *Water Resour. Res.* **54**, 2183 (2018).
- [70] T. Le Borgne, M. Dentz, and J. Carrera, Lagrangian Statistical Model for Transport in Highly Heterogeneous Velocity Fields, *Phys. Rev. Lett.* **101**, 090601 (2008).
- [71] M. Dentz and D. Bolster, Distribution-Versus Correlation-Induced Anomalous Transport in Quenched Random Velocity Fields, *Phys. Rev. Lett.* **105**, 244301 (2010).
- [72] P. K. Kang, M. Dentz, T. Le Borgne, and R. Juanes, Spatial Markov Model of Anomalous Transport Through Random Lattice Networks, *Phys. Rev. Lett.* **107**, 180602 (2011).
- [73] Y. Méheust and J. Schmittbuhl, Flow enhancement of a rough fracture, *Geophys. Res. Lett.* **27**, 2989 (2000).
- [74] M. B. Cardenas, D. T. Slottke, R. A. Ketcham, and J. M. Sharp, Navier-Stokes flow and transport simulations using real fractures shows heavy tailing due to eddies, *Geophys. Res. Lett.* **34**, L14404 (2007).
- [75] T. Le Borgne, J.-R. de Dreuzy, P. Davy, and O. Bour, Characterization of the velocity field organization in heterogeneous media by conditional correlation, *Water Resour. Res.* **43**, W02419 (2007).
- [76] P. K. Kang, Q. Lei, M. Dentz, and R. Juanes, Stress-induced anomalous transport in natural fracture networks, *Water Resour. Res.* **55**, 4163 (2019).
- [77] A. A. Balkema and L. De Haan, Residual life time at great age, *Ann. Probabil.* **2**, 792 (1974).
- [78] J. Pickands III, Statistical inference using extreme order statistics, *Ann. Stat.* **3**, 119 (1975).
- [79] J. Beirlant, Y. Goegebeur, J. Segers, and J. L. Teugels, *Statistics of Extremes: Theory and Applications* (John Wiley & Sons, New York, 2006).
- [80] S. Coles, *An Introduction to Statistical Modeling of Extreme Values* (Springer, New York, 2001).
- [81] P. K. Kang, M. Dentz, T. Le Borgne, S. Lee, and R. Juanes, Anomalous transport in disordered fracture networks: Spatial Markov model for dispersion with variable injection modes, *Adv. Water Resour.* **106**, 80 (2017).
- [82] T. Sherman, A. Fakhari, S. Miller, K. Singha, and D. Bolster, Parameterizing the spatial Markov model from breakthrough curve data alone, *Water Resour. Res.* **53**, 10888 (2017).
- [83] A. Massoudieh and M. Dentz, Upscaling non-linear reactive transport in correlated velocity fields, *Adv. Water Resour.* **143**, 103680 (2020).
- [84] J. Hyman, M. Dentz, A. Hagberg, and P. K. Kang, Linking structural and transport properties in three-dimensional fracture networks, *J. Geophys. Res.* **124**, 1185 (2019).
- [85] R. J. Twiss, G. M. Protzman, and S. D. Hurst, Theory of slickenline patterns based on the velocity gradient tensor and microrotation, *Tectonophysics*. **186**, 215 (1991).
- [86] M. M. Mielnik, R. P. Ekatpure, L. R. Sætran, and F. Schönfeld, Sinusoidal crossflow microfiltration device—Experimental and computational flowfield analysis, *Lab Chip* **5**, 897 (2005).
- [87] L. J. Perez, J. J. Hidalgo, and M. Dentz, Upscaling of mixing-limited bimolecular chemical reactions in Poiseuille flow, *Water Resour. Res.* **55**, 249 (2019).